Version of Record: https://www.sciencedirect.com/science/article/pii/S0098300420306191
Manuscript_c8902cb66c400e13fcb1728a66d6dc8b

REAL-TIME WATER LEVEL MONITORING USING LIVE CAMERAS AND COMPUTER VISION TECHNIQUES

Navid H. Jafari, Ph.D.
Department of Civil and Environmental Engineering
Louisiana State University
Email: njafari@lsu.edu

Xin Li, Ph.D.
School of Electrical Engineering and Computer Science
Louisiana State University
Email: xinli@lsu.edu

Qin Chen, Ph.D.
Department of Civil and Environmental Engineering
Department of Marine and Environmental Sciences
Northeastern University
Email: q.chen@northeastern.edu

Can-Yu Le
Department of Computer Science
Xiamen University
Email: ranger.lcy@gmail.com

Logan P. Betzer
Staff Engineer
Evans-Graves Engineers, Inc.
Email: lbetzer@evans-graves.com

Yongqing Liang
School of Electrical Engineering and Computer Science
Louisiana State University
Email: ylian16@lsu.edu

A paper submitted for RE-REVIEW and possible publication in the *Computer and Geosciences* Journal.

September 28, 2020

© 2020 published by Elsevier. This manuscript is made available under the Elsevier user license
https://www.elsevier.com/open-access/userlicense/1.0/

Real-Time Water Level Monitoring using Live Cameras and Computer Vision Techniques

Navid H. Jafari[1], Xin Li[2], Qin Chen[3], Can-Yu Le[4,2], Logan P. Betzer[1], Yongqing Liang[2]

ABSTRACT: Characterizing urban hydrographs during rain storms, hurricanes, and river floods is important to decrease loss of lives and assist emergency responders with mapping disruptions to operation of major cities. High water marks, stream gages, and rapidly deployed instrumentation are the current state-of-practice for hydrological data during a flood event. The objective of this study was to develop technology that can provide accurate and timely flood hydrographs while harnessing the Big Data generated from videos and images. In particular, levels are predicted from images by using reference objects as a scale. The novelty of this work involved leveraging object-based image analysis (OBIA), which used image segmentation training algorithms to differentiate areas of images or videos. In particular, the deep learning-based semantic segmentation technique was trained using images from an MIT database along with images compiled from traffic cameras and the experiments and a case study. The fully convolutional network was used for image segmentation and subsequent object labeling. This algorithm was applied to a laboratory and two field experiments before demonstration at Buffalo Bayou in Houston, TX during Hurricane Harvey. The laboratory and field experiments indicated that the image segmentation technique was reproducible and accurate from a controlled environment to rain storms and localized flooding in small streams on the LSU campus. Moreover, the segmentation algorithm successfully estimated flood levels in Buffalo Bayou in downtown Houston, Texas during Hurricane Harvey. This signifies that if time-lapse imagery is available, this algorithm- and program-estimated water elevations can provide insight to the hydrograph and spatial inundation during flooding from rainstorms or hurricanes.

Keywords: Hydrology; Algorithms; Computer Graphics; Image Analysis; Data Processing; Floods

[1] Dept. of Civil and Environmental Engineering, Louisiana State University (LSU), Baton Rouge, LA 70803. Email: njafari@lsu.edu, lbetze1@lsu.edu.

[2] School of Electrical Engineering and Computer Science, LSU, Baton Rouge, LA 70803. Email: xinli@lsu.edu, ylian16@lsu.edu.

[3] Dept. of Civil and Environmental Engineering and Dept. of Marine and Environmental Engineering, Northeastern University, Boston, MA 02115. Email: q.chen@northeastern.edu.

[4] Dept. of Computer Science, Xiamen University, Xiamen, China. Email: ranger.lcy@gmail.com.

1. INTRODUCTION

Major rain storms and hurricanes, such as Hurricanes Katrina in 2005; Sandy in 2012; Harvey, Irma, and Maria in 2017; and Florence in 2018; can cause flooding events that disrupt operations of major cities and result in physical infrastructure, social, and economic damages. Magnitude of high water and duration found in hydrographs during these extreme flood events correlate to the extent of these damages. Currently, high water marks and stream gages provide hydrological data, along with debris lines found on structures. For instance, the U.S. Geological Survey (USGS) and Federal Emergency Management Agency (FEMA) collected flood data from 2,123 high water marks and 40 USGS stream gages throughout Texas following Hurricane Harvey. This information is important because it assists officials in updating building codes, planning evacuation routes, creating floodplain management ordinances, providing environmental assessments and planning other community efforts to become more flood-resilient (Lu et al., 2018; Rani et al., 2018; Watson et al., 2018; Xiao et al. 2018). However, continuous flood hydrographs are difficult to construct given only the information from water marks and stream gages (Calvo and Savi, 2009; Xing et al., 2018). For example, high water marks and debris lines only describe the water elevation at its peak, but it lacks information about the duration of the event, the time of day of peak water levels, or the rate at which the water level rose or fell. When temporal sequence of water level information is available, these signals can be modeled and used to interpolate and extrapolate (predict) the spatial and temporal expanse of flood inundation (Ghorbani et al., 2010; Kisi et al., 2012; Maheswaran and Khosa, 2013), for geographic visualization (Kulkarni et al., 2014), simulations (Chen et al., 2018), and flood warning system for emergency evacuation and response (Wang et al., 2018).

Water related data can also be obtained from different sources, such as sensors mounted on stream gages (Ghorbani et al., 2010; Kisi et al., 2012, Maheswaran and Khosa, 2013), airborne sensing (Li et al., 2010), satellite imagery (Kulkarni et al., 2014), wireless sensor networks and geographic information (Horita et al. 2015), and various social media and crowdsourcing data (Wang et al., 2018). Stream gages provide more data on these characteristics, but these instruments are often installed far from the flooded areas of interest to relay accurate and real-time data to emergency operation centers. This dearth of data available for flood hydrograph reconstruction is hampering communities to learn from past events in order to become resilient towards future floods, hurricanes, and sea level rise. Accordingly, the impetus for this study stems from the realization that big datasets of time-lapse videos and images are created every day, including traffic monitoring, private and public security, and social media. For example, the Houston TRANSTAR system consists of approximately 900 cameras that continuously streams live footage. These images are publicly accessible through the internet and hence represent a rich data source if water levels can be extracted from reference objects using computer vision techniques.

Extracting water level information from image and video data is nontrivial because it is inherently difficult to segment water. Thus, this work aims to tackle this problem by advancing object-based image analysis (OBIA) techniques. OBIA has been previously applied in conjunction with aerial photography for vegetation classification and urban feature identification, along with damage analysis, disaster management, and risk management (Blaschke, 2010; Garcia et al., 2018; Lee and Yang 2018; Bandini, 2017). Van der Sande et al. (2003) also classified land use in the villages of Itteren and Borgharen in The Netherlands to create a floodplain friction map for use with flood models. Beyond the current applications, this paper describes a novel methodology to estimate water elevations by leveraging time-lapse photos and OBIA. To achieve this objective, two control laboratory experiments and three flood events in bayous and canals around the Louisiana State University (LSU) campus were conducted to develop hydrographs for method verification. A segmentation algorithm was developed to automatically label the water and gage from these experiments. Manually estimated water levels were used to verify the accuracy of the segmentation algorithm and program. To establish the applicability to natural hazards, the segmentation algorithm was subsequently used to estimate flood levels in Buffalo Bayou in downtown Houston, Texas during Hurricane Harvey. The algorithm- and program-estimated water elevations were recorded as hydrographs and compared to in-situ measurements and nearby stream gages. With a validated methodology, the societal impact is immense because databases of time-lapse camera images can be collected and analyzed in near real-time to provide insight to the rise and fall of water levels and spatial coverage during flooding from rainstorms or hurricanes.

2. RELATED WORK

2.1. Contour Detection through Image Segmentation

To automatically segment and extract the contours of the flood and reference objects from an image, a program is needed to outperform semantic segmentation or instance segmentation. Semantic segmentation is the process of automatically labeling regions on each pixel of an image with the category name of the recognized object. Instance segmentation proceeds one step further to distinguish each individual object rather than just a category. Classic image segmentation methods (Alvarez et al., 2010; Barrow and Tenenbaum, 1981; Grady, 2006; Kass et al., 1988; Roerdink and Meijster, 2000) often identify a specific object contour using manually designed features, i.e., color change or its gradient, with a regularization through geometric or elastic smoothness. These methods are often sensitive to initial guess and image noise, as they are easily impeded by local minima. More recent use of deep learning-based algorithms permits extraction of more abstract and robust features that capture local and global characteristics, significantly out performing traditional methods. The most widely adopted deep learning-based semantic segmentation framework comes from the fully convolutional network (FCN) (Long et al., 2015), which trains a series of convolutional layers to extract features and then uses a new deconvolutional operation to upsample the feature vector to infer pixelwise category. Commonly adopted convolutional neural network (CNN) architectures in feature extractors are AlexNet (Krizheysky et al., 2012), VGG16 (Smionyan and Zisserman, 2014), and ResNet (He et al., 2016). Earlier methods (e.g., Hariharan et al., 2014) generated segmentation candidates and extracted features for each candidate, then used a support vector machine (SVM) to classify the candidates by their features into corresponding categories. A widely adopted strategy (Arnab, 2017; Bai, 2017; Liu, 2017) starts from semantic segmentation results (e.g., output from FCN), then partitions pixels of the same category into different instances based on their spatial positions.

A video is a sequence of images with strong temporal coherency. Consecutive frames are similar and contents only undergo small and continuous deformations. By exploiting this implicit continuity assumption, the robustness of semantic segmentation can be improved but with extra constraints (i.e., computationally expensive). Thus, the current focus in this study is on reducing computation complexity by finding a balance between segmentation accuracy and algorithm efficiency. Shelhamer et al. (2016) indicates that the semantic contents of a scene usually evolve slowly, and the output of deeper layers are more stable than shallower layers. Therefore, a schedule scheme can integrate information in the previous frames into the interface of CNNs. The Deep Feature Flow introduced in Zhu (2017) designs a feature propagation function to transfer features in previous frames to the next, leading to a significant improvement in segmentation efficiency.

Another category of semantic video segmentation algorithm exploits temporal consistency across frames to improve the prediction accuracy, such as post-segmentation refinement where upon the FCN-computed segmentation results (Chen et al., 2018a; Lin 2017; Zhu, 2017) and temporal smoothness constraints can be adopted to refine and optimize the segmentation. For example, Kundu et al. (2016) define the dense 3D (2D+Time) conditional random field (CRF) on frame blocks, where a random field will be optimized to assign spatially and temporally consistent labeling to each pixel. Generic neural network architectures in Nilsson (2018), Hu (2018), and Chen (2018b) propose to propagate information from previous several frames to the current frame. However, this approach needs dense labeling data (e.g., pixel-wise labeled videos) to train the network. Such labeled flood video datasets are not available, and manually generating a sufficient dataset is laborious. Therefore, the aim of this study is to design a spatiotemporal smoothness model that can refine semantic segmentation results by using temporal smoothness and prior knowledge. The developed system is anticipated to work without needing a significant volume of labeled flood data.

2.2. Applications of Image Segmentation in Geoscience

Image segmentation is gaining significant attention in geoscience research and practical applications because it can be used for object identification and target description. In particular, automatic image segmentation helps us to reduce tedious work such as manual labeling for processing remote sensing images. Vasuki et al. (2017) developed an interactive image segmentation tool for lithology boundary detection from photographic images of rock surfaces. Chen et al. (2018) designed an optimal path clustering algorithm to segment remote sensing land cover images for scene classification. Jasiewicz et al. (2018) proposed a multi-scale seeded region growing algorithm to segment large-sized land cover images for Earth Observation (EO) data analysis. However, these methods are usually built based on traditional segmentation algorithms, such as region growing (Jasiewicz et al., 2018), region merging (Vasuki et al., 2017), and clustering (Chen et al., 2018). They are not sufficiently robust when handling water data that contains complex heterogeneous texture and illumination contrast. Karimpouli and Tahmasebi (2019) built a deep convolutional autoencoder to segment digital rock images. Deep learning based image segmentation can be helpful in handling the aforementioned challenges. But when processing temporal flood footage data, lighting conditions and water appearance change dramatically over space and time, making segmentation from a single scene extremely challenging (e.g., Fig. 4(a)). Integrating temporal consistency constraint (see discussion in Section 3.3) is critical to improve the robustness of segmentation. Techniques developed in this work are general and applicable to other geoscience applications.

3. IMAGE PROCESSING METHODOLOGY

3.1 Overview

A learning-based semantic segmentation undergoes two stages, i.e., training and segmentation. The training data may include images sampled from video footage, other general images captured by traffic cameras, or found on the Internet. These images can provide different views of the site using different cameras under different illuminations. More diverse training images can require a more complex network and more datasets to train but also provide a more generalizable program to work more stably with various images. In contrast, if the system is used to analyze a certain type of scene, an image corpus with smaller variance can be designed. This method makes the network easier to train but less generalizable to different images or videos. An ever-growing flood labeling database can effectively support the training of deep networks for general flood recognition and segmentation.

The semantic segmentation module discussed herein is based on FCN (Long et al., 2015), where an auto-encoder consisting of an encoder and a decoder was built. The encoder utilizes general image classification networks that extract feature maps from original images. The decoder uses a series of deconvolutional layers to restore a labeled image back to its original size. Then, each pixel is assigned into a specific class. After training the network, new images or videos can be fed to automatically get a pixelwise segmentation (labeling) result. A flood region and common reference objects (staff gage, pillar, guardrail, or traffic pole) can be identified and segmented from the background. However, the raw segmentation results may contain some noise especially in regions with ambiguous colors, which leads to incorrect labeling. The temporal consistency is utilized to refine the segmentation result to get a more stable and accurate segmentation.

From the segmented flood contour and the reference object, the height of the reference object above the water level is estimated using the ratio of pixel heights. The pixel height of an object is defined as the vertical height difference from the highest pixel of the reference object down to the water interface. The submerged ratio is calculated by:

$$x = 1 - \frac{h_t}{h_0} \tag{1}$$

where h_0 is the original pixel height of the reference object before submergence and h_t is the new pixel height at time t. The details of converting the pier height from pixel to actual length is further explained in Section 5.2

3.2 Training Semantic Segmentation

Existing labeled images are used to train an FCN network for flood segmentation. Datasets from ADE20K (Zhou et al., 2016, 2017) containing about 1,888 water/flood images were used as initial training datasets. During training, data augmentation was incorporated to increase the robustness of the model, including random brightness disturbance, random hue color disturbance, random contrast disturbance, and random affine transformation. In practice, this model can handle moderate changing such as aperture and white balance. The collected images were also manually annotated and added as additional system training. Fig. 1 illustrates the architecture of the auto-encoder. Initially, an image is fed into the encoder (i.e., the feature extractor). The encoder consists of a series of convolutional layers and outputs a feature vector. The decoder contains several deconvolutional operations, receives the feature vector, and outputs a 3-dimensional volume whose width and height match the original image resolution and the depth n equals the number of classification.

Given an image of resolution $U \times V$ and a list L of labels to consider, the output of the decoder is a tensor $Y_{U \times V \times |L|}$. The prediction on a pixel (u, v), denoted as $y_{u,v}$, is an L -dimensional vector and $y_{u,v,l}$ indicates the prediction score or likelihood of pixel (u, v) being assigned label l. During the training phase, the loss function is defined using a *softmax* cross entropy and an L_2 regularization term:

$$loss = \sum_{u,v} \left(-\sum_{t=l_o}^{l_n} \hat{y}_{u,v,t} \log \sigma(y_{u,v})_t + k \|\theta\|^2 \right) \quad (2)$$

$$\hat{y}_{u,v,t} = \begin{cases} 1, \text{pixel } u, v \text{ should be labeled as } l \\ 0, \text{otherwise} \end{cases} \quad (3)$$

$$\sigma(y_{u,v})_t = \frac{exp(y_{u,v,l})}{\sum_{r \in \{l_o,\ldots,l_n\}} \exp(y_{u,v,r})} \quad (4)$$

where (*u, v*) is the pixel position, $y_{u,v}$ is the output prediction vector on this pixel, *{l*$_0$, . . . , l_n*}* is the set of considered labels, and ***θ*** indicates all the trainable parameters in the network. $y\hat{}_{u,v,l}$ contains the groundtruth labeling information, whose value is 1 if pixel (*u, v*) should be assigned label *l* and 0 otherwise. $\sigma(y_{u,v})_l \in [0, 1]$ is the softmax function which normalizes the raw inference value $y_{u,v,l}$ to a value in [0, 1], and can be considered as the probability of (*u, v*) being labeled *l*. This loss function penalizes the inconsistency between the pixelwise prediction and the groundtruth label. The regularization term suppresses large parameters, which usually lead to overfitting. With such a network trained on this dataset, it is used to generate the segmentation on given images. Fig. 2 shows an example of semantic segmentation result on the Buffalo Bayou flood video. The color-encoded labels overlay the original image for better visualization. The blue and yellow regions correspond to detected water and piers, respectively.

3.3 Segmentation Refinement using Temporal Smoothness

The aforementioned semantic segmentation only considers a given image itself, without considering its previous and next frames. Noisy signals are often inevitable. In the flood application, rain, wind, and lighting can all contribute to unstable imaging. Furthermore, rain drops can fall on the camera and blur a portion of the video for a period of time. These outliers can severely affect the semantic segmentation on single images. On the other hand, if the input is a video, there is strong correlation between consecutive frames, and temporal consistency across adjacent frames provides us useful constraints to refine the individually segmented objects (either the flood region or the reference object). Intuitively, it is necessary to consider several consecutive frames together and ensure the tracked object contours remain stable. Fig. 3 illustrates this mechanism where temporal smoothness constraint is enforced in each temporal block that consists several consecutive images. Each image and its preceding K frames form its overlapping temporal block (illustrated in a colorful oval), and this image segmentation will be refined using segmentations from other images in this block.

Two temporal smoothness constraints were designed to refine an image semantic segmentation using its associated block. The first is the contour trajectory smoothness constraint. Contours segmented in the last K frames are used to evaluate the stability of current frame segmentation. For example, if $K = 1$ for the current image frame I_t, the previous frame I_{t-1} is considered, where the subscripts and -1 are time indices. The direct image segmentation result of I_t is denoted as $_t$. A temporal blending is first conducted to obtain a new segmentation $_t$:

$$S'_t = (1-\lambda) * S'_{t-1} + \lambda * S_t \tag{5}$$

Another threshold results in the final smoothed segmentation $_t$:

$$S'_t = T(S'_t, \alpha, 1) \tag{6}$$

where the variable is a decay rate that controls the historical segmentation influence (in this study $= 0.2$), α is a binarization threshold (in this study, $\alpha = 0.5$), T is the binary threshold function that returns 1 for pixels whose intensity is greater than α, and returns 0 otherwise. The λ is the decay rate, which controls the historical segmentation influence. Lower λ indicates a higher weight/impact from the previous results. The benefit of using this propagation model is that the impact of the prior segmentation can disappear smoothly. The setting of hyper-parameter λ is affected by the video frame rate, as well as the flood and scene variation conditions. If the flood changes rapidly or the frame rate is low, λ is larger to decrease the influence of previous frames.The second constraint is the prior constraint. If there are multiple consecutive outlier frames, or an outlier's contour is highly abnormal, only enforcing trajectory smoothness constraint is insufficient. For example, during the night at the Buffalo Bayou in Fig. 4, the dark environment results in significant difficulty to track the contour of the raising water and hence is continuously unreliable. Therefore, a model is needed that can understand prior knowledge. In particular, a threshold is specified to provide a physical constraint on the rise and fall of the hydrograph based on engineering judgement. In this case, it is assumed the water level change within every minute is usually less than 1 ft (30.5 cm). Converting this value to the video pixel, a detector is used to monitor the estimated height and identify abnormal perturbation. In the Buffalo video, the interval between two consecutive frames is one minute (Fig. 4). Hence, an estimate is made to understand which change is unlikely true and thus treated as an outlier. A Laplacian detector detects sudden changes in water level estimation for each frame. The estimation outliers are refined following the prior constraint. Fig. 4 illustrates an example of this temporal smoothing. Fig. 5 shows the Buffalo hydrographs before and after refinement using temporal smoothness. The superimposed yellow regions are segmented water. The direct image segmentation result in Fig. 4(a) contains multiple incorrectly identified regions (highlighted in red boxes). After applying temporal smoothness, the segmentation in Fig. 4(b) becomes more stable and accurate.

The experiments demonstrate that the aforementioned constraints can stably segment water contours from collected videos. Meanwhile, more advanced (also more computationally expensive) temporal smoothness models can be adopted. For example, the CRF in Kundu et al. (2016) is adopted to model this temporal consistency. In each overlapping temporal block (Fig. 3), a CRF is built to balance each pixel classification (image segmentation result) and similarity between pixel pairs (spatial and temporal smoothness of segmentation in a video). CRF was implemented and adopted as the temporal smoothness model and found that its performance is only slightly better than the current model. However, CRF is time-consuming and often takes hundreds of CPU hours to converge. Therefore, the current less complicated spatiotemporal smoothness model is adopted which can already produce desirable results from obtained videos. For example, the GPU memory requirement is 3.3 GB for training, where the computation time is 150 seconds per epoch. For segmentation, the GPU memory requirement is 4.8 GB, and the computation time is 15 frames per second. The total training time is about 5 hours. The smoothing step runs quickly (10 seconds).

4. LABORATORY AND FIELD CALIBRATION

The images used for labeling and algorithm development were collected from controlled laboratory and field experiments on the LSU campus, specifically at two streams referred to as Bayou Fountain and Corporation Canal (Fig. 6). Bayou Fountain runs on the west side of campus and is fed by drainage from the campus. It is 2.5 m wide where water levels are typically less than 30 cm, and a stream gage allows validation the labeled images. Corporation Canal starts in downtown Baton Rouge and runs across the east side of campus and into Bayou Duplantier. Due to their large drainage areas, both bodies of water are known to rise significantly during intense rain events, making them prime locations to test the new methodology proposed.

4.1 Laboratory Control Experiments

The control laboratory experiments involved a water tank and a meter stick to use as a water level reference gage (Fig. 7), and the electrical tape of 15.24 cm length provided a control for the program to automatically label. Using a Brinno TLC200 Pro time-lapse camera capturing images every 1 second, water was poured into the water tank at varying rates to create a hydrograph with varying slopes to test the robustness of the labeling algorithm. The Brinno camera automatically creates a time-lapse video so the images used for labeling were extracted using the program *video2image.py*. Using the *labelme* program, the water in the first image was traced with a polygon and labeled as water, as was the labeled ruler and staff gage (Fig. 7). The *transfer_label.py* program transfers the first polygons and labels to subsequent images, which reflects the change in water level. Photos were labeled at five second intervals to accurately capture the hydrographs and to train the program to automatically label the remaining frames of the laboratory videos. In Fig. 8, the virtual gage hydrograph (blue circle and green square symbols) refer to the segmentation, which used the labeled images. The predictions were validated by manually measuring the water elevations of non-labeled images (red triangles and purple diamonds). In particular, Fig. 8 shows that the program-estimated water levels from the laboratory control experiments closely matches those that were manually measured (RMSE ~ 0.13 cm). The value of ΔE~ 0.25 cm gives the largest difference between the virtual gage and validation values for the laboratory control experiments. Thus, the controlled experiments demonstrated that the program was working with precision and accuracy, which permitted testing to expand to controlled field experiments along two streams on the LSU campus.

4.2 Field Experiments

For the rain event on 18 May 2018 at Bayou Fountain, a waterproof Brinno camera was mounted across the stream gage to capture images every minute for 64 minutes. The Brinno camera in Fig. 9(a) demonstrated limited focus capabilities (maximum resolution 1280x720 pixels), leaves and other debris masked the stream bank from the water, and rain droplets gathered on the waterproof casing which blurred many of the images (Fig. 9b). The images were still used to test the accuracy of the labeling program in a noisy environment, i.e., water level is not easily distinguished due to debris or image quality. However, the Brinno TLC200 Pro was replaced with the Moultrie S-50i game camera (resolution 1920×1080 pixels) to evaluate the labeling accuracy with another camera and overcome the resolution and raindrop issues (Fig. 9(c) compares Moultrie and Brinno cameras). The Moultrie camera captured images from rain events on 11 and 12 June 2018. Images were captured every 30 seconds for 121 minutes on July 11, while the June 12 rain event images were captured at 30 second intervals for 20 minutes. The latter duration was significantly shorter because the intense precipitation caused the stream to overflow and submerge the Moultrie camera. Following Bayou Fountain, another Moultrie S-50i game camera was attached to a bridge timber pile at Corporation Canal to provide additional images for labeling and to verify the algorithm for another site under different environmental conditions. An existing stream gage attached to a bridge pier measures the water level starting at 1.83 m (6 ft) above the bottom of the canal (Fig. 10a).

The same procedure to label the laboratory experiments was used for the Brinno camera at Bayou Fountain. The Moultrie camera also followed the labeling process (Fig. 10b), with one less step because this camera directly provides images. Because the rise and fall of water levels during rain events took hours, the images from Bayou Fountain on 18 May were labeled at a 4 minute interval and the images on 11 June were labeled at 5 minute intervals. The images from

Bayou Fountain on 12 June 2018 were labeled every minute and images from Corporation Canal were labeled at 2 minute intervals. The intervals of labeled images were selected based on the duration of rain and rise of the flood hydrograph. The May 18 and June 11 Bayou Fountain hydrographs extended for approximately 55 minutes and 120 minutes, respectively, while the June 12 Corporation Canal hydrograph was only 20 minutes. The water levels from Bayou Fountain on June 12 were less accurately labeled by the program, as the camera switched to the nighttime infrared setting due to the low-light conditions. This caused a switch from color to black and white images and hence the water and stream bank did not sufficiently contrast to train the program.

The manually labeled images were used to train the program to automatically label the remaining frames of the field experiment videos. The results in Fig. 11 show the comparison between the virtual gage and manually evaluated images for validation. The greatest difference between the manually-estimated and virtual gage water elevations was less than 5 cm. This occurred during the May 18 Bayou Fountain event (Fig. 11a) because of rain drops on the Brinno lens clouding the images, debris in the water and on the bank making the water line indistinguishable, and lower resolution of the Brinno camera. Fig. 11(a) also suggests that the switch from the Brinno to Moultrie camera allowed the automatic segmentation program to more accurately detect and estimate the water levels in Bayou Fountain and Corporation Canal. In particular, the water levels only differed by an average of 2 cm and a maximum of 5 centimeters. For example, the RMSE for the Brinno camera during the May 18 experiment was 2 cm, while the RMSE for the Moultrie cameras were 0.9 cm and 1.2 cm at Bayou Fountain and Corporation Canal, respectively. Therefore, the increased image resolution from 720p to 1080p and lack of raindrops collecting on the lens of the camera alleviated the problems encountered on May 18.

Following June 11 and 12, the segmentation algorithm was refined using images from the three experiments, which permitted re-evaluation of the images from the May 18 Bayou Fountain event (see green squares in Fig. 11a). With the updated algorithm, the RMSE was reduced from 2 cm to 0.4 cm and the greatest difference between the virtual gage and validation points decreased to 0.9 cm. The results from the laboratory and field experiments verified the accuracy of the segmentation algorithm and labeling program. These techniques were next applied to a case study at Buffalo Bayou in downtown Houston during Hurricane Harvey.

5. CASE STUDY OF HOUSTON FLOODING DURING HURRICANE HARVEY

5.1 Background

Hurricane Harvey made landfall at San Jose Island along the Texas coast on 25 August 2017 as a Category 4 hurricane. Rain gages in Houston recorded over 76.2 cm (30 inches) of rainfall over the region during the week that the cyclone looped over southeastern Texas. This major storm caused catastrophic flooding of the densely-populated regions of Houston and Beaumont (Blake and Zelinsky, 2018). Inland rivers that drain into the Gulf of Mexico, such as the Colorado, Guadalupe, and Brazos Rivers, were overwhelmed by floodwaters, leading to flooded major interstate highways, such as I-10 and I-45 (Blake and Zelinsky, 2018). In particular, Buffalo Bayou flows from Katy, TX through Houston and into the Gulf of Mexico via Galveston Bay (Buffalo Bayou Partnership, 2018). Data obtained from stream gages and high-water marks along Buffalo Bayou reveal the severity of flooding in Houston during Hurricane Harvey. The USGS identified multiple high-water marks from Harvey in Sesquicentennial Park near Buffalo Bayou (USGS Flood Event Viewer, 2018). Fig. 12 shows the locations of the high-water marks (see blue squares). A high-water mark on the northern bank of Buffalo Bayou revealed a water elevation of 10.3 m (33.7 ft) NAVD88, while a debris line on the southern bank marked an elevation of 11.9 m (39.1 ft) NAVD88. USGS also reported a peak stage of 10.3 m (33.7 ft) NAVD88 on 1 September 2017 at 17:00 (5:00 pm).

The Harris County Flood Control District measures water levels throughout the county using stream gages. In particular, Buffalo Bayou is monitored by seven stream gages spanning from Barker Reservoir to Burnett Bay. During Hurricane Harvey, these stream gages captured high water levels in the channel. Located 4 km west of the camera location, the Shepherd Drive stream gage reported a peak water elevation of 11.8 m (38.8 ft) on 28 August 2017, approximately 12.8 m (42 ft) above the bottom of the stream bed. At Milam Street, the rising floodwaters reached an elevation of 8.3 m (27.1 ft) on 27 August 2017, a water level of 11.3 m (33.85 ft) above the bottom of bayou (Harris Country Flood Warning System, 2017). However, the stream gage at Milam Street only collected data until 02:44 (2:44 am) on August 27. This gage failure demonstrates the need for multiple methods to construct and verify flood hydrographs.

5.2 Hurricane Harvey Image Analysis

During Hurricane Harvey, a time-lapse camera was placed on the second floor of the Bayou Place Offices building on Capitol Street near Milam Street (see Fig. 12 for general location and Fig. 13b for exact location). The camera overlooked Buffalo Bayou, Memorial Drive overpass, Interstate 45 overpass, and the Houston Aquarium. The camera recorded the rise and fall of flood levels in Buffalo Bayou from approximately 16:00 (4:00 pm) on Friday, August 25 to 03:00 (3:00 am) on Wednesday, August 30. Although the Harrison County Flood Control District stream gage at Milam Street does not report water levels after 02:44 (2:00 am) on Sunday, August 27, the camera observed flood waters continuing to rise and overtopping Memorial Drive overpass by 09:30 (9:30 am) later that morning.

The video of Buffalo Bayou during Hurricane Harvey was analyzed using semantic segmentation to create a hydrograph. In particular, images were extracted each second to form a near continuous hydrograph. The algorithm used an I-45 bridge pier adjacent to Buffalo Bayou as a reference object and created a hydrograph to show the ratio of the bridge pier submerged by water (see yellow rectangle in Fig. 13a). Buffalo Bayou and the bridge pier were surveyed by T. Baker Smith, LLC to determine the elevations of the bottom of the channel and the bottom and top of the pier using a Leica TS02 Total Station (Fig. 13c). The elevations of the pier at ground surface and at the top were 0.83 m (2.72 ft) NAVD88 and 18.1 m (59.41 ft) NAVD88, respectively. The total length of the bridge pier is 17.28 m (57.5 ft). To calculate the elevation of the water, the submerged ratio was converted to a distance from the bottom of the pier using Eq. (7). The submerged ratio refers to the ratio of pixels water covered pixels to visible pixels in the image segmentation program.

$$\text{Water Elevation (m, NAVD88)} = 0.83\,\text{m} + 17.28\,\text{m} \times (\text{submerged ratio}) \qquad (7)$$

The reconstructed hydrograph in Fig. 14 was compared to the Milam Street stream gage, which is the closest information available on Buffalo Bayou. In particular, the Milam stream gage shows an initial rise and fall of the hydrograph on August 26, which was visually verified with the Buffalo Bayou video. This first rise is likely related to the first impulse of the floodwaters arriving in Houston. Approaching midnight of August 26, the Milam gage hydrograph begins to rapidly rise until the instrument failed at an elevation of 8 m NAVD88 in the morning of August 27. In comparison, the image segmentation algorithm developed herein shows fluctuations in water level at an elevation 1 to 3 m in the evening of August 25 and early morning of August 26. During the daylight, image segmentation successfully captures the Milam Street hydrograph starting around 12:00 on August 26, i.e., the two lines are in close agreement in Fig. 14. When the Milam Street gage fails, the image segmentation provides continuous information on the flood waters. For example, the peak flood level of approximately 14 m occurred on the night of August 27 to morning of August 28. The water level started to rapidly decrease on August 28 to about 9 m before slightly rising to 10.5 m by the early morning of August 29. During August 29, flood levels in Buffalo Bayou decreased to approximately 3 m. After August 30, Buffalo Bayou remained at a constant water level of 3 m, which was verified with other stream gages upstream (Shepherd Drive and San Felipe Drive) that indicated waters remained relatively high for an extended duration into early 2 September 2017. The sharp decline in the segmentation analysis in the early morning of August 27 is because of the difficulty in labeling images at night, especially if limited lighting is available and reflectance of light on water is present. As natural light increased from sunrise, the image segmentation method self-corrected and continued to provide reasonable results during the course of the remaining flood event. Though, it is evident that the water level fluctuations mostly occur at night. Nevertheless, Fig. 14 demonstrates the image segmentation methodology developed and implemented in this study is capable of capturing a flood hydrograph.

6. SUMMARY AND CONCLUSIONS

Measuring and disseminating real-time water levels in urban environments during rain storms, hurricanes, and river floods is paramount to ensuring human safety and assisting in mapping disruptions to the operation of major cities that result in physical infrastructure, social, and economic damages. High water marks, stream gages, and rapidly deployed instrumentation currently provide hydrological data during a flood event. The impetus of this study was to develop technology that can provide accurate and timely water levels while harnessing the Big Data generated from videos and images posted by individuals on social media, YouTube, and permanent infrastructure such as road traffic cameras. This Big Data facilitates creation of a high-fidelity spatial-temporal map of flooding that does not currently exist.

The techniques presented in this study involves using reference objects in videos and images to estimate water levels with time. The novelty of this work involved leveraging object-based image analysis (OBIA), which used image segmentation training algorithms to differentiate areas of images or videos. In particular, the deep learning-based semantic segmentation technique was trained using images from an MIT database along with images compiled from traffic cameras and the experiments and case study presented herein. The FCN was used for image segmentation and subsequent object labeling. This algorithm was applied to a laboratory and two field experiments before demonstration at Buffalo Bayou in Houston, TX during Hurricane Harvey. The field experiments indicated that the image segmentation technique was reproducible and accurate from a controlled environment to rain storms and localized flooding in small streams on the LSU campus. Moreover, the segmentation algorithm successfully estimated flood levels in Buffalo Bayou in downtown Houston, Texas during Hurricane Harvey. This signifies that if time-lapse imagery is available, this algorithm- and program-estimated water elevations can provide insight to the hydrograph and spatial inundation during flooding from rainstorms or hurricanes. Future work with this technique includes the need to resolve image analyses at night, remove effects of rainfall on camera lenses, and developing a system to collect images during extreme events. Moreover, this technique can be harnessed to larger data streams (e.g., Houston traffic cameras and local security cameras) to develop near real-time water levels in urban environments that can allow emergency operation centers to make informed decisions on emergency response and disaster recovery.

To better tackle nighttime images, dark image enhancing and contrast enhancing algorithms can be adopted to preprocess the dark images. The mutual coherence between daytime images and nighttime images will be explored such that the structures extracted from the daytime images can guide the segmentation of nighttime images. The model also learns the appearance of the water based on the training images. In this current compiled training dataset, photos containing water with turbulence, debris, among others were not specifically the objective. Such types of water videos and images represent the next steps in this research investigation. Raindrops often harm the segmentation results, as those regions can be misidentified. However, this effect can be currently diminished by the proposed temporal blending and the prior constraints. Moreover, if wind gusts alter the position of a camera, the water segmentation component is still reliable because the classification of each pixel is based on extracted features and their matching with ones in previous frames. This is not sensitive to camera tilt/shift. The water level estimation can be affected if the reference object can move. A future direction to tackle this issue is to register all the frames to the coordinates of the first initial frame. If the reference object becomes lost, the estimation can proceed using another reference object. Future work will collect more labeled flood datasets and will explore more advanced but inexpensive models to more flexibly incorporate high-level temporal information to achieve reliable segmentation in complex and noisy scenes.

ACKNOWLDGEMENTS

This material is based upon work supported by the National Science Foundation under Grant No. (#1760582). The authors would like to thank Louisiana Sea Grant Undergraduate Research Opportunities Program (UROP), T. Baker Smith, Inc., and Louisiana Board of Regents Industrial Ties Research Program for supporting this research. The support of Qin Chen provided by Northeastern University Global Resilience Institute is also gratefully acknowledged. We appreciate permission by Mr. Teddy Vandenberg to use his time-lapse video of Buffalo Bayou during Hurricane Harvey. Any opinions, findings, and conclusions or recommendations expressed in this material are those of the author(s) and do not necessarily reflect the views of the National Science Foundation, T. Baker Smith, Louisiana Board of Regents, and Louisiana Sea Grant.

COMPUTER CODE AVAILABILITY

There are two sets of codes used in this study. The first code was Pytorch-FCN, which we used as a starting point for developing our codes, and it was develop by Ketaro Wada in 2017. The second source code was developed by the LSU team in 2018. It is called LSU Water Segmentation and the developers are Xin Li, Yongqing Liang, and Can-Yu Le. The contact information for all of these authors is provided at the beginning of the manuscript. The required hardware is a typical computer (Windows, Apple, Linux), where the required software and programming language are Python. Program size is minimal, possibly one (1) MB. The authors developed our segmentation algorithm and program based on the open-source library FCN by

Ketaro Wada (https://github.com/wkentaro/pytorch-fcn). The LSU code can be accessed at https://github.com/xmlyqing00/LSUWaterSegmentation.

AUTHORSHIP STATEMENT

Professors Navid Jafari, Qin Chen, and Xin Li developed the research idea and paper. Professor Jafari led the writing of the manuscript, with assistant from Professors Chen and Li. Professor Li with graduate students Can-Yu Le and Yongqing Liang developed the algorithm and code and performed the segmentation analyses for the paper. Undergraduate student Logan Betzer conducted the laboratory and field experiments and prepared manuscript figures.

REFERENCES

Ali Ghorbani, M., Khatibi, R., Aytek, A., Makarynskyy, O., & Shiri, J. (2010). Sea water level forecasting using genetic programming and comparing the performance with Artificial Neural Networks. *Computers & Geosciences, 36*(5), 620-627. doi:10.1016/j.cageo.2009.09.014

Álvarez, L., L. Baumela, P. Henríquez, and P. Márquez-Neila (2010), Morphological snakes, paper presented at Computer Vision and Pattern Recognition (CVPR), 2010 IEEE Conference on, IEEE.

Arnab, A., and P. H. Torr (2017), Pixelwise instance segmentation with a dynamically instantiated network, paper presented at CVPR.

Bai, M., and R. Urtasun (2017), Deep watershed transform for instance segmentation, paper presented at 2017 IEEE Conference on Computer Vision and Pattern Recognition (CVPR), IEEE.

Bandini, F., J. Jakobsen, D. Olesen, J. A. Reyna-Gutierrez, and P. Bauer-Gottwein (2017), Measuring water level in rivers and lakes from lightweight Unmanned Aerial Vehicles, *Journal of Hydrology*, *548*, 237-250, doi:https://doi.org/10.1016/j.jhydrol.2017.02.038.

Barrow, H. G., and J. M. Tenenbaum (1981), Interpreting line drawings as three-dimensional surfaces, *Artificial intelligence*, *17*(1-3), 75-116.

Blake, E. S., and D. A. Zelinsky (2018), NATIONAL HURRICANE CENTER TROPICAL CYCLONE REPORT HURRICANE HARVEY*Rep. AL092017*.

Blaschke, T. (2010), Object based image analysis for remote sensing, *ISPRS Journal of Photogrammetry and Remote Sensing*, *65*(1), 2-16, doi:https://doi.org/10.1016/j.isprsjprs.2009.06.004.

Calvo, B., and F. J. N. H. Savi (2009), Real-time flood forecasting of the Tiber River in Rome, *50*(3), 461-477, doi:10.1007/s11069-008-9312-9.

Chen, L.-C., G. Papandreou, I. Kokkinos, K. Murphy, and A. L. Yuille (2018), Deeplab: Semantic image segmentation with deep convolutional nets, atrous convolution, and fully connected crfs, *IEEE transactions on pattern analysis and machine intelligence*, *40*(4), 834-848.

Chen, S., Sun, T., Yang, F., Sun, H., & Guan, Y. (2018). An improved optimum-path forest clustering algorithm for remote sensing image segmentation. *Computers & Geosciences, 112*, 38-46. doi:10.1016/j.cageo.2017.12.003

Chen, Y., J. Pont-Tuset, A. Montes, and L. Van Gool (2018), Blazingly Fast Video Object Segmentation with Pixel-Wise Metric Learning, paper presented at Proceedings of the IEEE Conference on Computer Vision and Pattern Recognition.

Chen, Z., Chen, N., Du, W., & Gong, J. (2018). An active monitoring method for flood events. *Computers & Geosciences, 116*. doi:10.1016/j.cageo.2018.04.009

Harris County Flood Control District (2018), Harris County Flood Warning System, edited.

García, Y. G., M. Shadaydeh, M. Mahecha, and J. J. N. H. Denzler (2018), Extreme anomaly event detection in biosphere using linear regression and a spatiotemporal MRF model, 1-19.

Grady, L. (2006), Random walks for image segmentation, *IEEE transactions on pattern analysis and machine intelligence*, *28*(11), 1768-1783.

Hariharan, B., P. Arbeláez, R. Girshick, and J. Malik (2014), Simultaneous detection and segmentation, paper presented at European Conference on Computer Vision, Springer.

He, K., G. Gkioxari, P. Dollár, and R. Girshick (2017), Mask r-cnn, paper presented at Computer Vision (ICCV), 2017 IEEE International Conference on, IEEE.

He, K., X. Zhang, S. Ren, and J. Sun (2016), Deep residual learning for image recognition, paper presented at Proceedings of the IEEE conference on computer vision and pattern recognition.

Horita, F. E. A., Albuquerque, J. P. D., Degrossi, L. C., Mendiondo, E. M., & Ueyama, J. (2015). Development of a spatial decision support system for flood risk management in Brazil that combines volunteered geographic information with wireless sensor networks. *80*, 84-94. doi:10.1016/j.cageo.2015.04.001

Hu, P., G. Wang, X. Kong, J. Kuen, and Y.-P. Tan (2018), Motion-Guided Cascaded Refinement Network for Video Object Segmentation, paper presented at Proceedings of the IEEE Conference on Computer Vision and Pattern Recognition.

Jasiewicz, J., Stepinski, T., & Niesterowicz, J. (2018). Multi-scale segmentation algorithm for pattern-based partitioning of large categorical rasters. *Computers & Geosciences, 118*, 122-130. doi:10.1016/j.cageo.2018.06.003

Karimpouli, S., & Tahmasebi, P. (2019). Segmentation of digital rock images using deep convolutional autoencoder networks. *Computers & Geosciences, 126*, 142-150. doi:10.1016/j.cageo.2019.02.003

Kass, M., A. Witkin, and D. Terzopoulos (1988), Snakes: Active contour models, *International journal of computer vision*, *1*(4), 321-331.

Kisi, O., Shiri, J., & Nikoofar, B. (2012). Forecasting daily lake levels using artificial intelligence approaches. *Computers & Geosciences, 41*, 169-180. doi:10.1016/j.cageo.2011.08.027

Krizhevsky, A., I. Sutskever, and G. E. Hinton (2012), Imagenet classification with deep convolutional neural networks, paper presented at Advances in neural information processing systems.

Kulkarni, A. T., Mohanty, J., Eldho, T. I., Rao, E. P., & Mohan, B. K. (2014). A web GIS based integrated flood assessment modeling tool for coastal urban watersheds. *64*, 7-14. doi:10.1016/j.cageo.2013.11.002

Kundu, A., V. Vineet, and V. Koltun (2016), Feature space optimization for semantic video segmentation, paper presented at Proceedings of the IEEE Conference on Computer Vision and Pattern Recognition.

Lee, C., and H. J. N. H. Yang (2018), A system to detect potential fires using a thermographic camera, *92*(1), 511-523.

Li, C., Shen, L., Wang, H.-B., & Lei, T. (2010). *The research on unmanned aerial vehicle remote sensing and its applications*.

Lin, G., C. Shen, A. Van Den Hengel, and I. Reid (2016), Efficient piecewise training of deep structured models for semantic segmentation, paper presented at Proceedings of the IEEE Conference on Computer Vision and Pattern Recognition.

Liu, S., J. Jia, S. Fidler, and R. Urtasun (2017), Sgn: Sequential grouping networks for instance segmentation, paper presented at The IEEE International Conference on Computer Vision (ICCV).

Long, J., E. Shelhamer, and T. Darrell (2015), Fully convolutional networks for semantic segmentation, paper presented at Proceedings of the IEEE conference on computer vision and pattern recognition.

Lu, C., J. Zhou, Z. He, and S. J. N. H. Yuan (2018), Evaluating typical flood risks in Yangtze River Economic Belt: application of a flood risk mapping framework, *94*(3), 1187-1210.

Maheswaran, R., & Khosa, R. (2013). Long term forecasting of groundwater levels with evidence of non-stationary and nonlinear characteristics. *52*, 422-436. doi:10.1016/j.cageo.2012.09.030

Nilsson, D., and C. Sminchisescu (2016), Semantic video segmentation by gated recurrent flow propagation, *arXiv preprint arXiv:1612.08871*, *2*.

Rani, M., S. Rehman, H. Sajjad, B. Chaudhary, J. Sharma, S. Bhardwaj, and P. J. N. H. Kumar (2018), Assessing coastal landscape vulnerability using geospatial techniques along Vizianagaram–Srikakulam coast of Andhra Pradesh, India, *94*(2), 711-725.

Roerdink, J. B., and A. Meijster (2000), The watershed transform: Definitions, algorithms and parallelization strategies, *Fundamenta informaticae*, *41*(1, 2), 187-228.

Shelhamer, E., K. Rakelly, J. Hoffman, and T. Darrell (2016), Clockwork convnets for video semantic segmentation, paper presented at European Conference on Computer Vision, Springer.

Simonyan, K., and A. Zisserman (2014), Very deep convolutional networks for large-scale image recognition, *arXiv preprint arXiv:1409.1556*.

United States Geological Survey (2018), USGS Flood Event Viewer, edited.

t3dwork (2017), Buffalo Bayou Timelapse During Harvey, edited.

Van der Sande, C. J., S. M. de Jong, and A. P. J. de Roo (2003), A segmentation and classification approach of IKONOS-2 imagery for land cover mapping to assist flood risk and flood damage assessment, *International Journal of Applied Earth Observation and Geoinformation*, *4*(3), 217-229, doi:https://doi.org/10.1016/S0303-2434(03)00003-5.

Vasuki, Y., Holden, E.-J., Kovesi, P., & Micklethwaite, S. (2017). An interactive image segmentation method for lithological boundary detection: A rapid mapping tool for geologists. *Computers & Geosciences, 100*, 27-40. doi:10.1016/j.cageo.2016.12.001

Wang, R.-Q., Mao, H., Wang, Y., Rae, C., & Shaw, W. (2018). Hyper-resolution monitoring of urban flooding with social media and crowdsourcing data. *Computers & Geosciences, 111*, 139-147. doi:10.1016/j.cageo.2017.11.008

Watson, K. M., Harwell, G. R., Wallace, D. S., Welborn, T. L., Stengel, V. G., & McDowell, J. S. (2018). *Characterization of peak streamflows and flood inundation of selected areas in southeastern Texas and southwestern Louisiana from the August and September 2017 flood resulting from Hurricane Harvey* (2328-0328)

Xiao, Y., B. Li, and Z. J. N. H. Gong (2018), Real-time identification of urban rainstorm waterlogging disasters based on Weibo big data, *94*(2), 833-842.

Xing, Y., Q. Liang, G. Wang, X. Ming, and X. J. N. H. Xia (2018), City-scale hydrodynamic modelling of urban flash floods: the issues of scale and resolution, 1-24.

Zheng, S., S. Jayasumana, B. Romera-Paredes, V. Vineet, Z. Su, D. Du, C. Huang, and P. H. S. Torr (2015), Conditional Random Fields as Recurrent Neural Networks, *arXiv e-prints*.

Zhou, B., H. Zhao, X. Puig, S. Fidler, A. Barriuso, and A. Torralba (2016), Semantic understanding of scenes through the ADE20K dataset, *arXiv preprint arXiv:1608.05442*.

Zhou, B., H. Zhao, X. Puig, S. Fidler, A. Barriuso, and A. Torralba (2017), Scene parsing through ade20k dataset, paper presented at Proceedings of the IEEE Conference on Computer Vision and Pattern Recognition, IEEE.

Zhu, X., Y. Xiong, J. Dai, L. Yuan, and Y. Wei (2017), Deep feature flow for video recognition, paper presented at CVPR.

LIST OF FIGURE CAPTIONS

Fig. 4. Segmentation refinement using temporal smoothness: (a) Raw segmentation result, (b) Temporal constraint (image permission from Teddy Vandenberg).

Fig. 5. Comparison between the original raw and refined water level estimations.

Fig. 6. Map of LSU campus where marked rectangles are the field experiment sites Bayou Fountain and Corporation Canal. Circles mark the camera locations.

Fig. 7. Labeled image from Brinno camera showing blue water to contrast yellow meter stick.

Fig. 8. Laboratory hydrographs developed from virtual gage.

Fig. 9. Field experiment at Bayou Fountain: (a) Visual of staff gage using Brinno TLC200 Pro camera, (b) Low quality image from Brinno camera due to raindrops, and (c) Visual of staff gage using Moultrie S-50i Game camera.

Fig. 10 Field experiment at Canal Corporation using Moultrie Camera: (a) Staff gage, and (b) Labeled image during June 12 event.

Fig. 11 Hydrographs created from estimated water levels: (a) May 18 at Bayou Fountain with Brinno camera and June 11 at Bayou Fountain with Moultrie camera, (b) June 12 at Corporation Canal with Moultrie camera.

Fig. 12 Overlay of downtown Houston and Buffalo Bayou with locations of (a) high water marks and (b) stream gages and camera location (image from Google Earth).

Fig. 13 Hurricane Harvey Case Study in Buffalo Bayou, Houston: (a) Camera location on Bayou Place Offices building, (b) Image of flooding Memorial Drive overpass from camera (image permission from Teddy Vandenberg), and (c) Survey of bridge pier and Buffalo Bayou by T. Baker Smith, LLC.

Fig. 14. Comparison of reconstructed hydrograph and Milam Street Stream Gage.

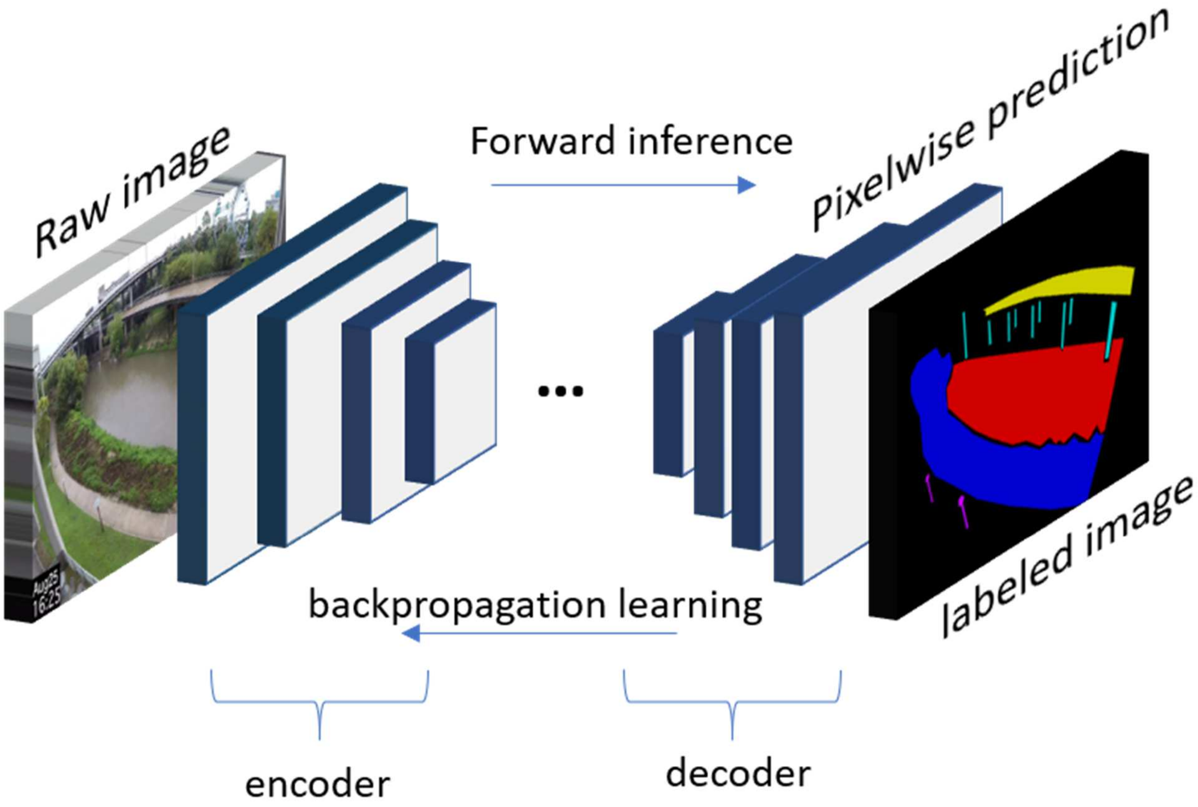

Figure 1. Semantic segmentation architecture based on the Fully Convolutional Network (FCN).

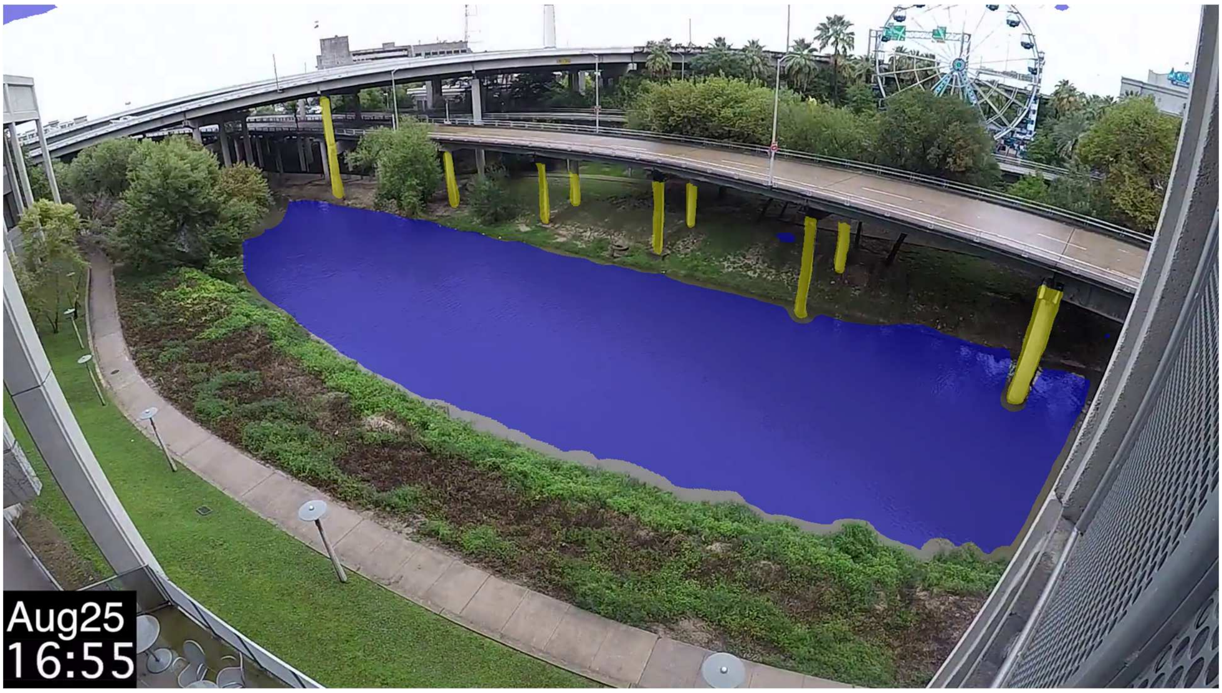

Figure 2. The semantic segmentation result on 16:55 August 25, 2017. The blue mask indicates water and the yellow mask indicates pier (image permission from Teddy Vandenberg).

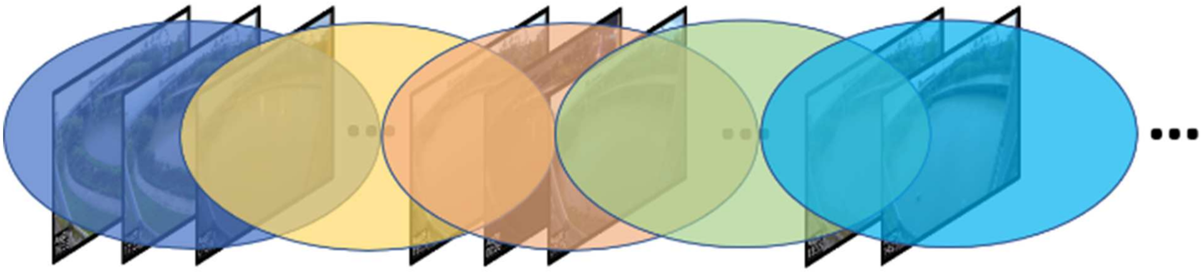

Figure 3. The structure of temporal smoothness consists of temporal blocks of several consecutive images. Each image and its preceding frames form its overlapping temporal block (illustrated in the colorful ovals). Image segmentation is refined using segmentations from other images in this block.

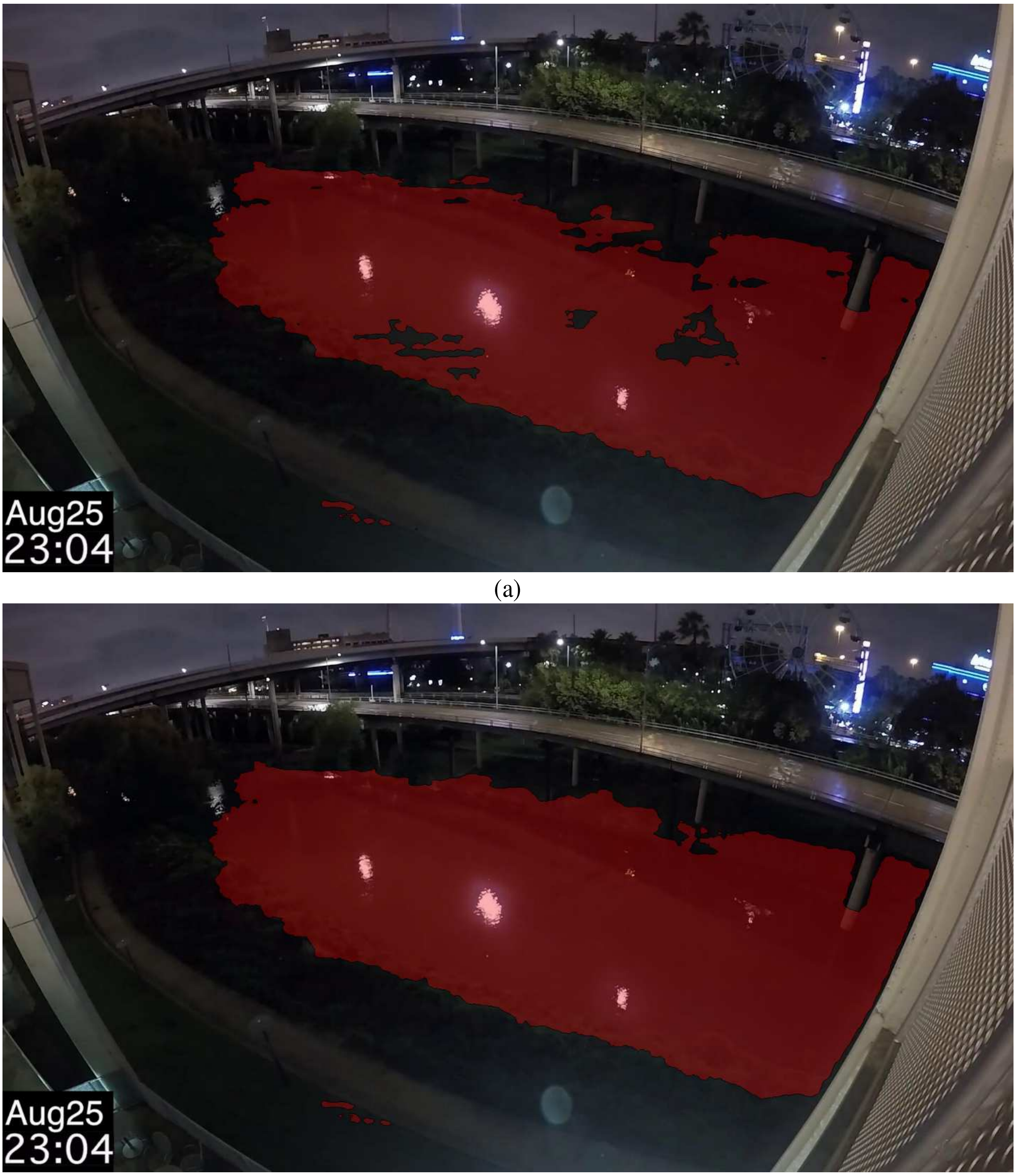

(a)

(b)

Figure 4. Segmentation refinement using temporal smoothness: (a) Raw segmentation result, (b) Temporal constraint (image permission from Teddy Vandenberg).

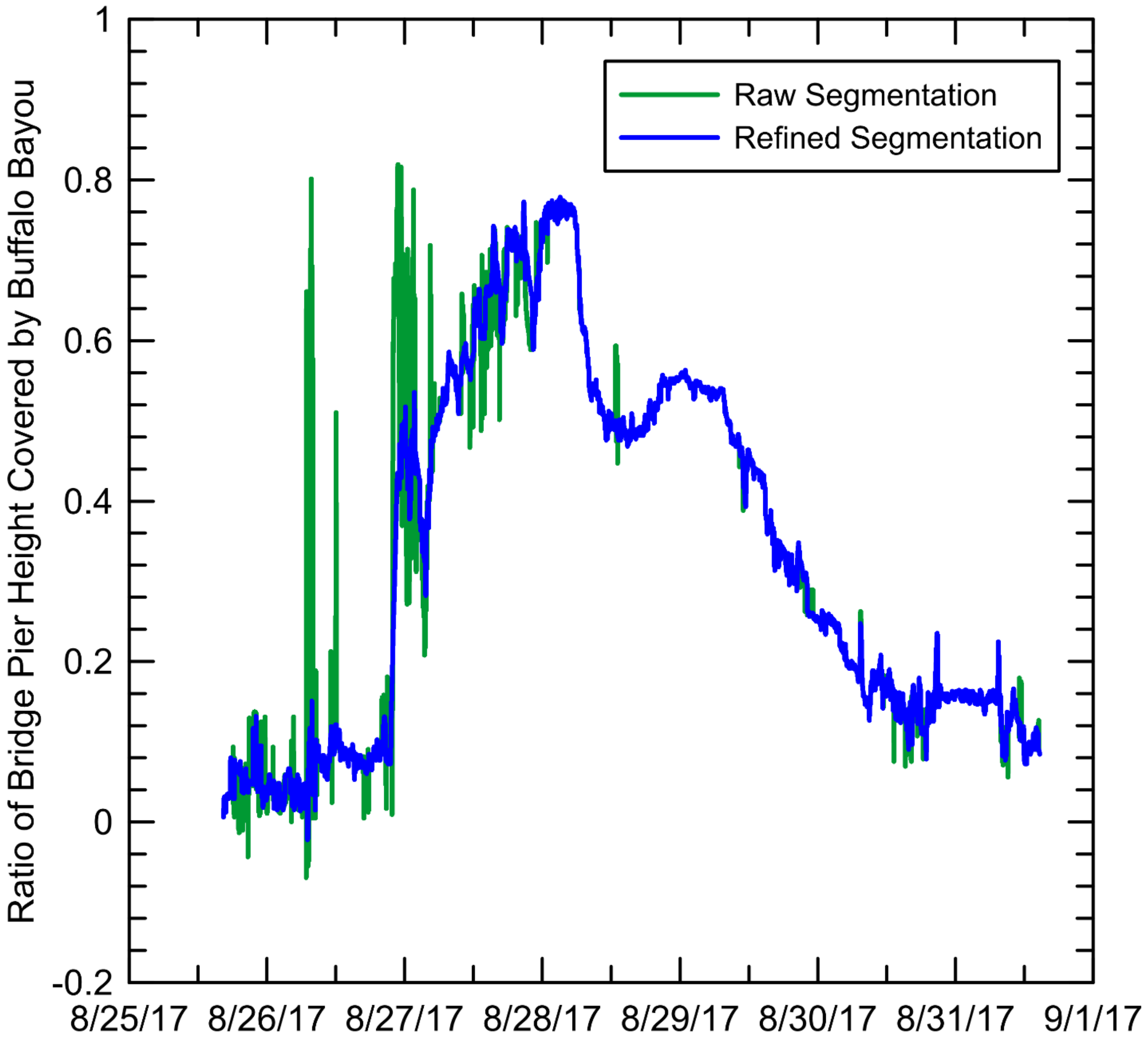

Figure 5. Comparison between the original raw and refined water level estimations.

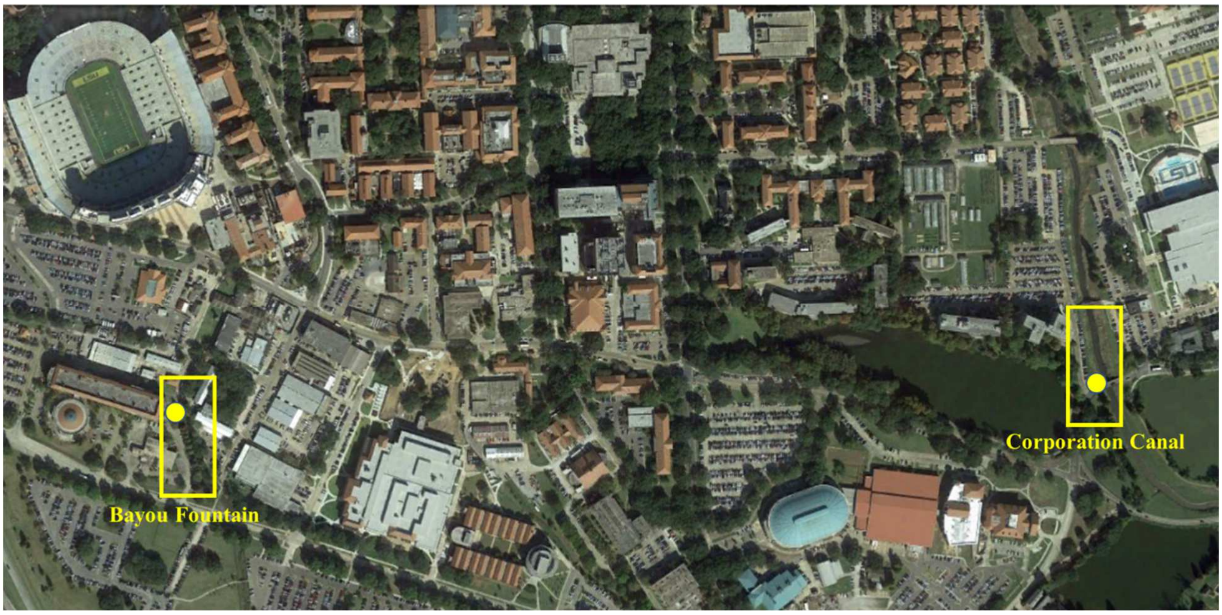

Figure 6. Map of LSU campus where marked rectangles are the field experiment sites Bayou Fountain and Corporation Canal. Circles mark the camera locations.

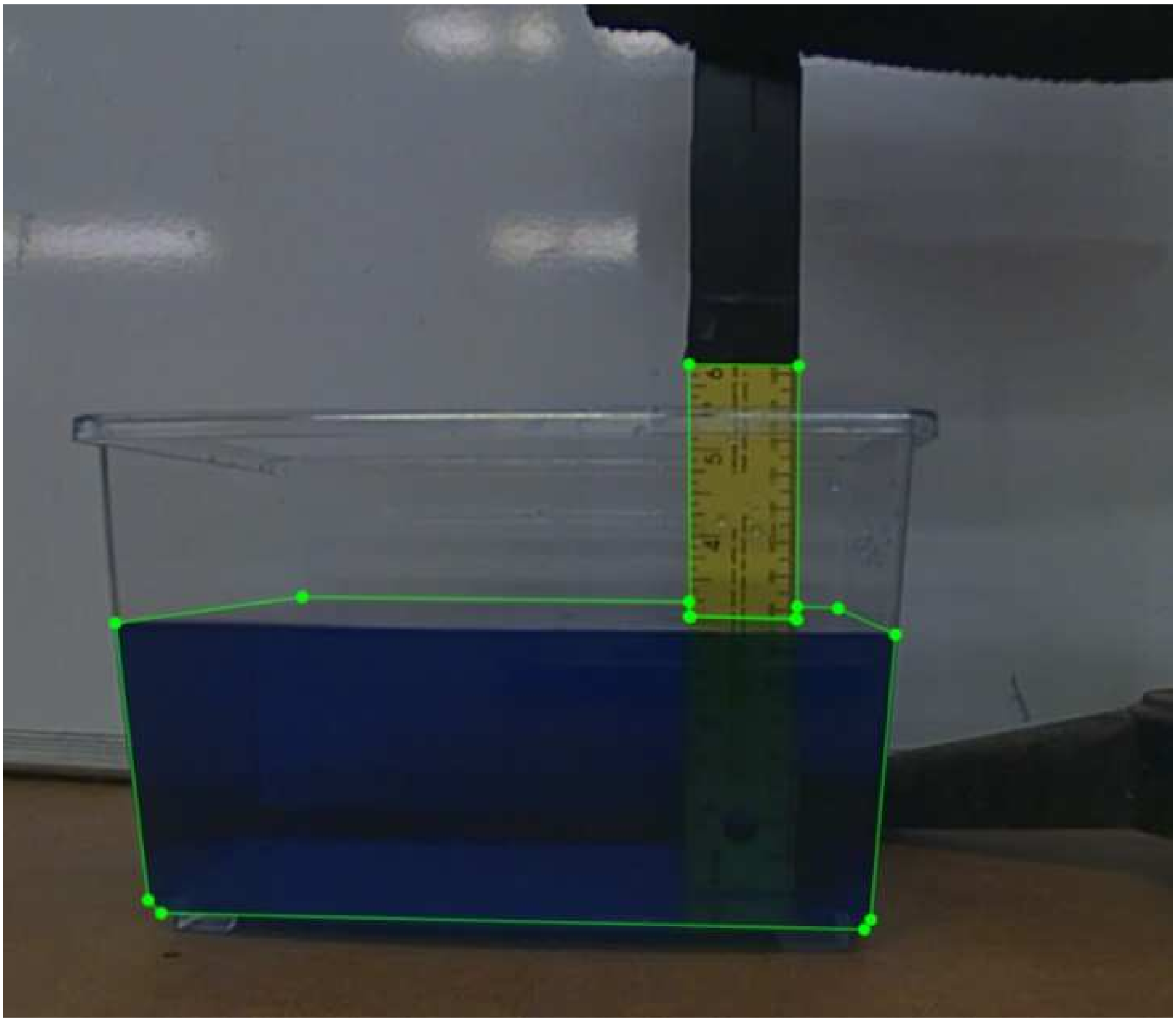

Figure 7. Labeled image from Brinno camera showing blue water to contrast yellow meter stick.

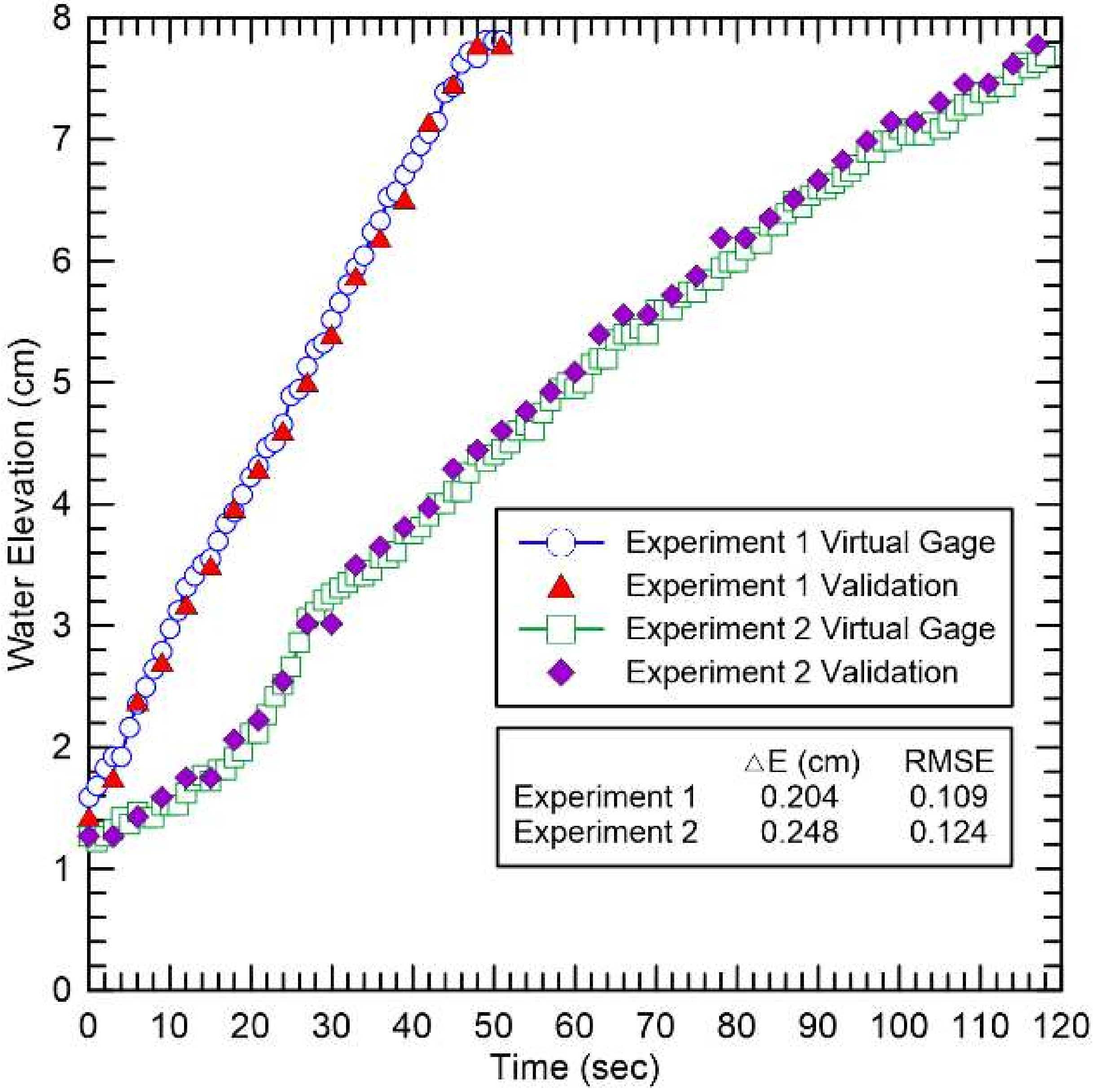

Figure 8. Laboratory hydrographs developed from virtual gage.

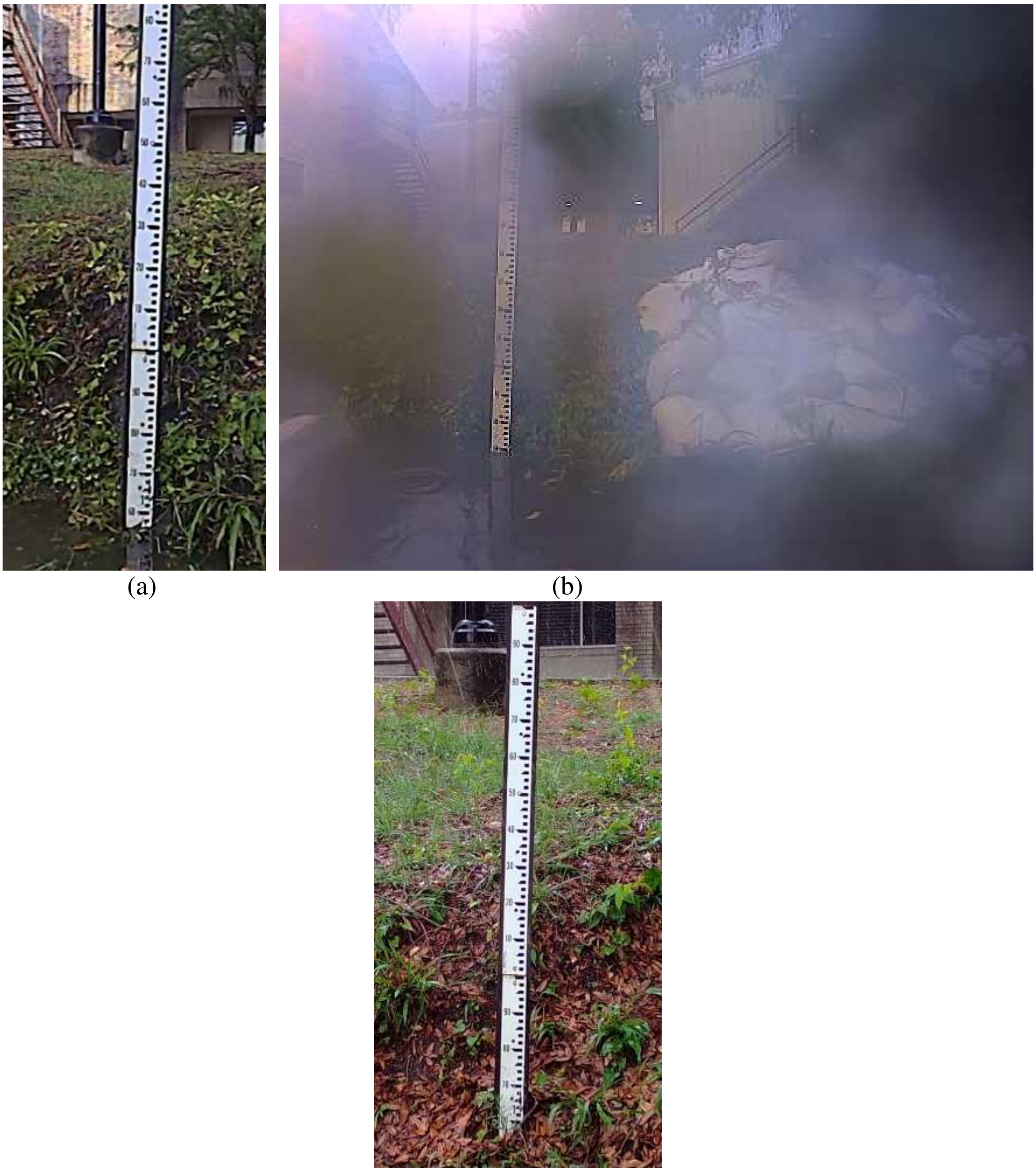

(a) (b)

(c)

Figure 9. Field experiment at Bayou Fountain: (a) Visual of staff gage using Brinno TLC200 Pro camera, (b) Low quality image from Brinno camera due to raindrops, and (c) Visual of staff gage using Moultrie S-50i Game camera.

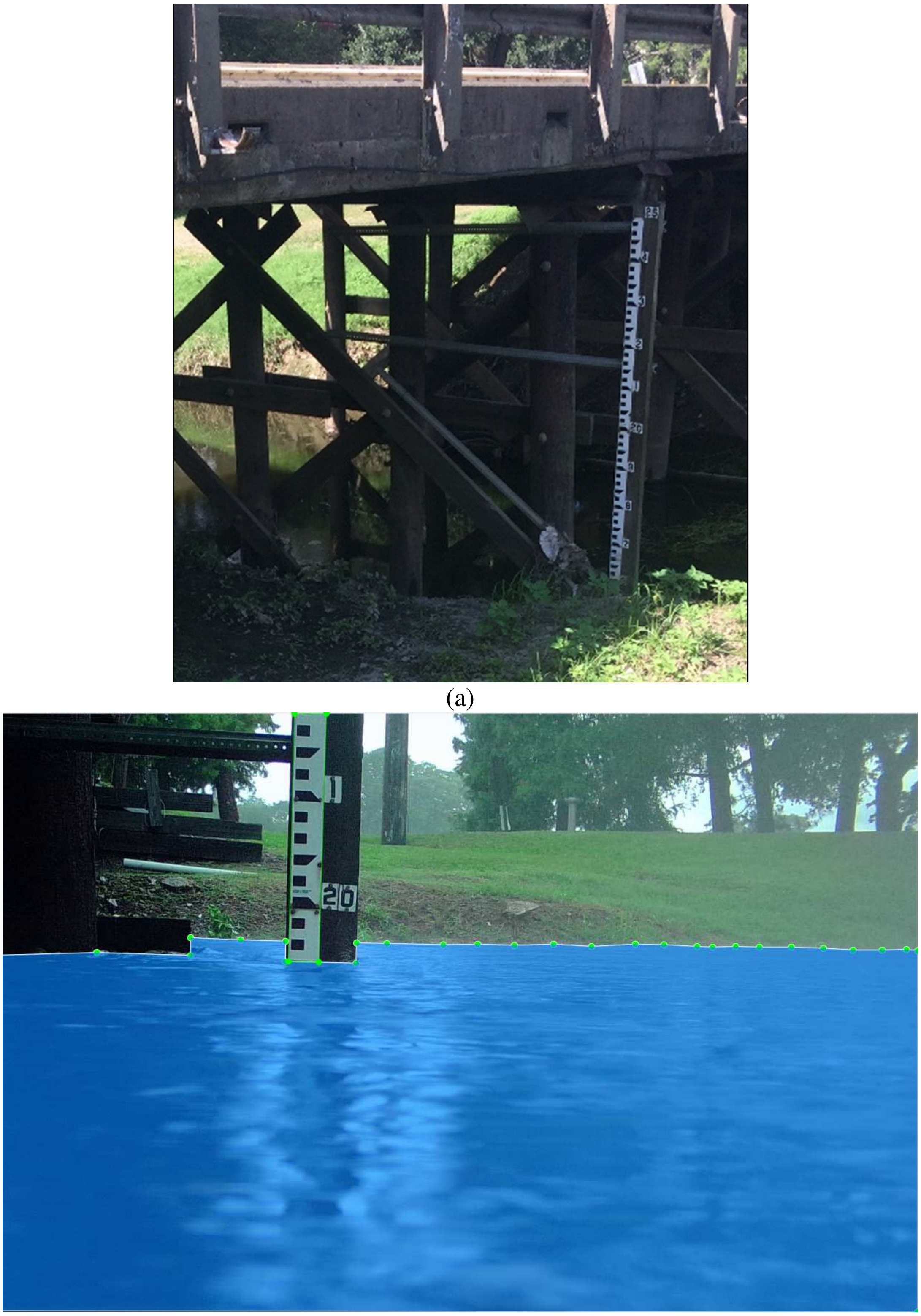

(a)

(b)

Figure 10. Field experiment at Canal Corporation using Moultrie Camera: (a) Staff gage, and (b) Labeled image during June 12 event.

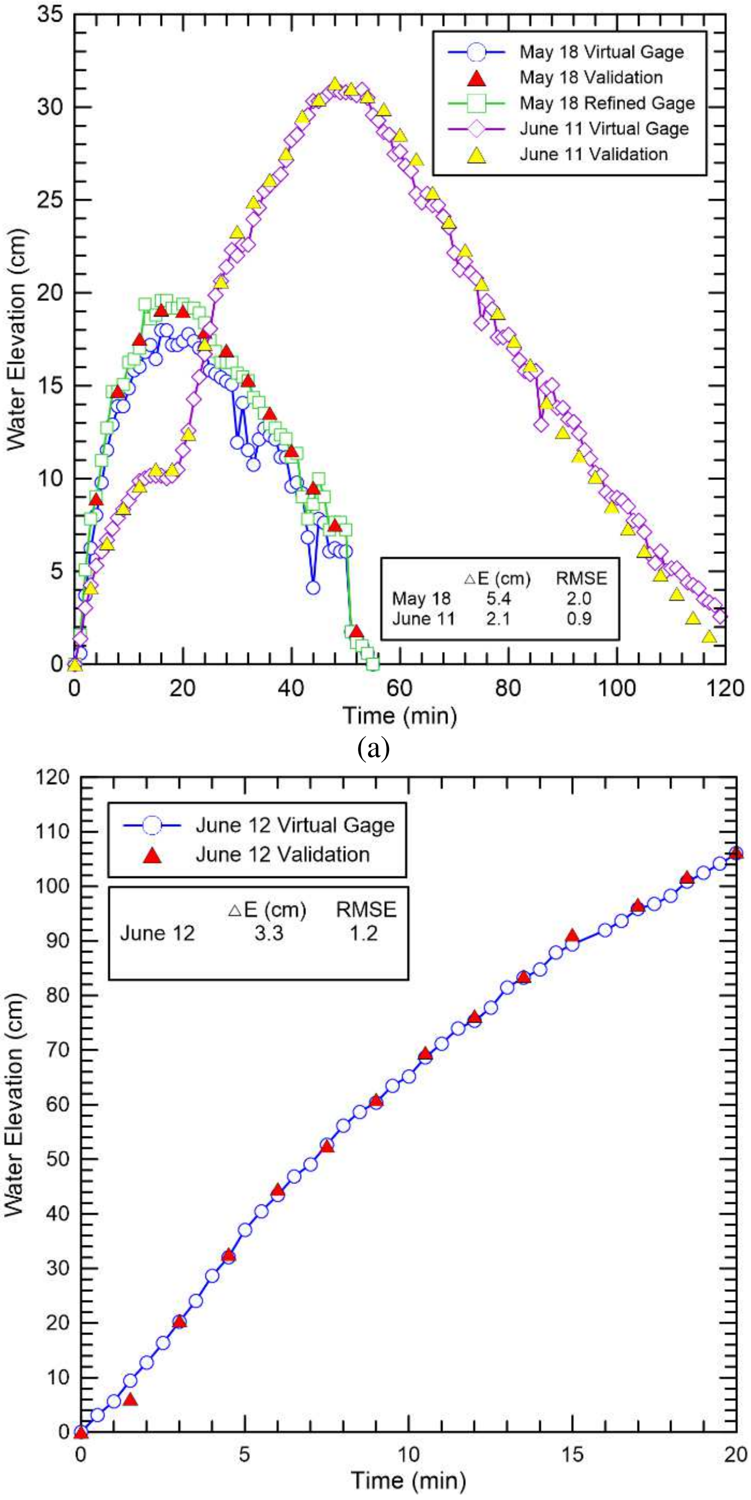

(a)

(b)

Figure 11. Hydrographs created from estimated water levels: (a) May 18 at Bayou Fountain with Brinno camera and June 11 at Bayou Fountain with Moultrie camera, (b) June 12 at Corporation Canal with Moultrie camera.

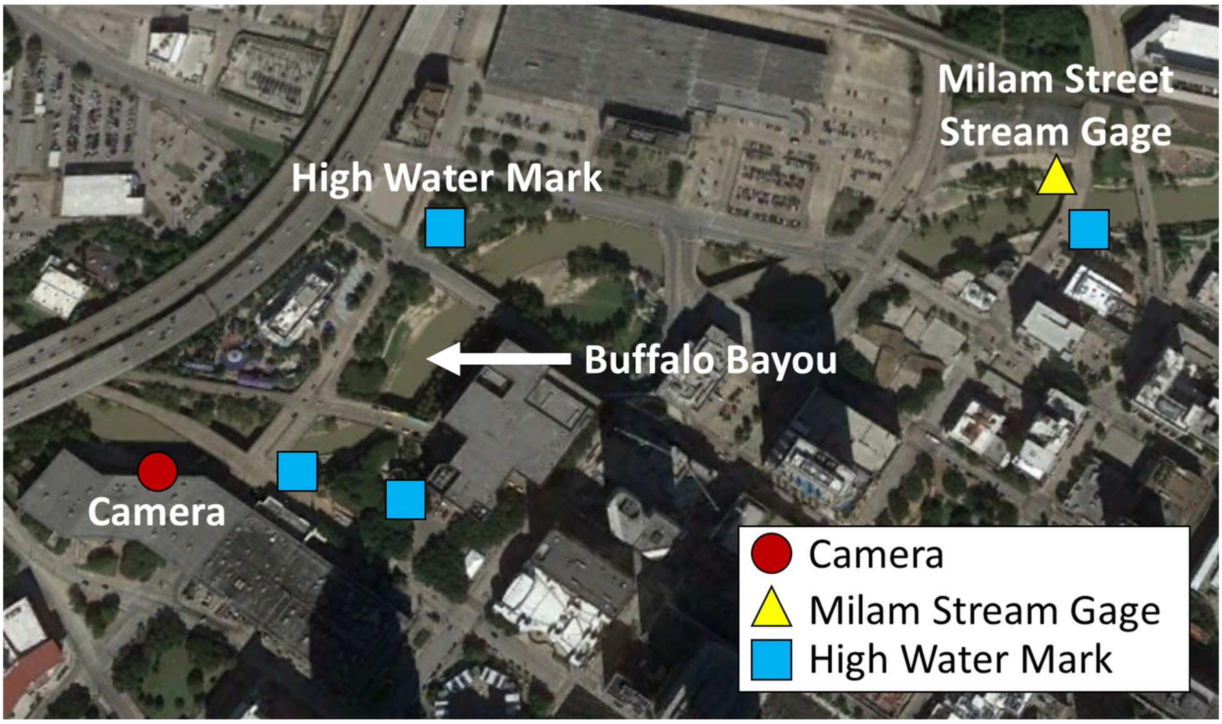

Figure 12. Overlay of downtown Houston and Buffalo Bayou with locations of (a) high water marks and (b) stream gages and camera location (image from Google Earth).

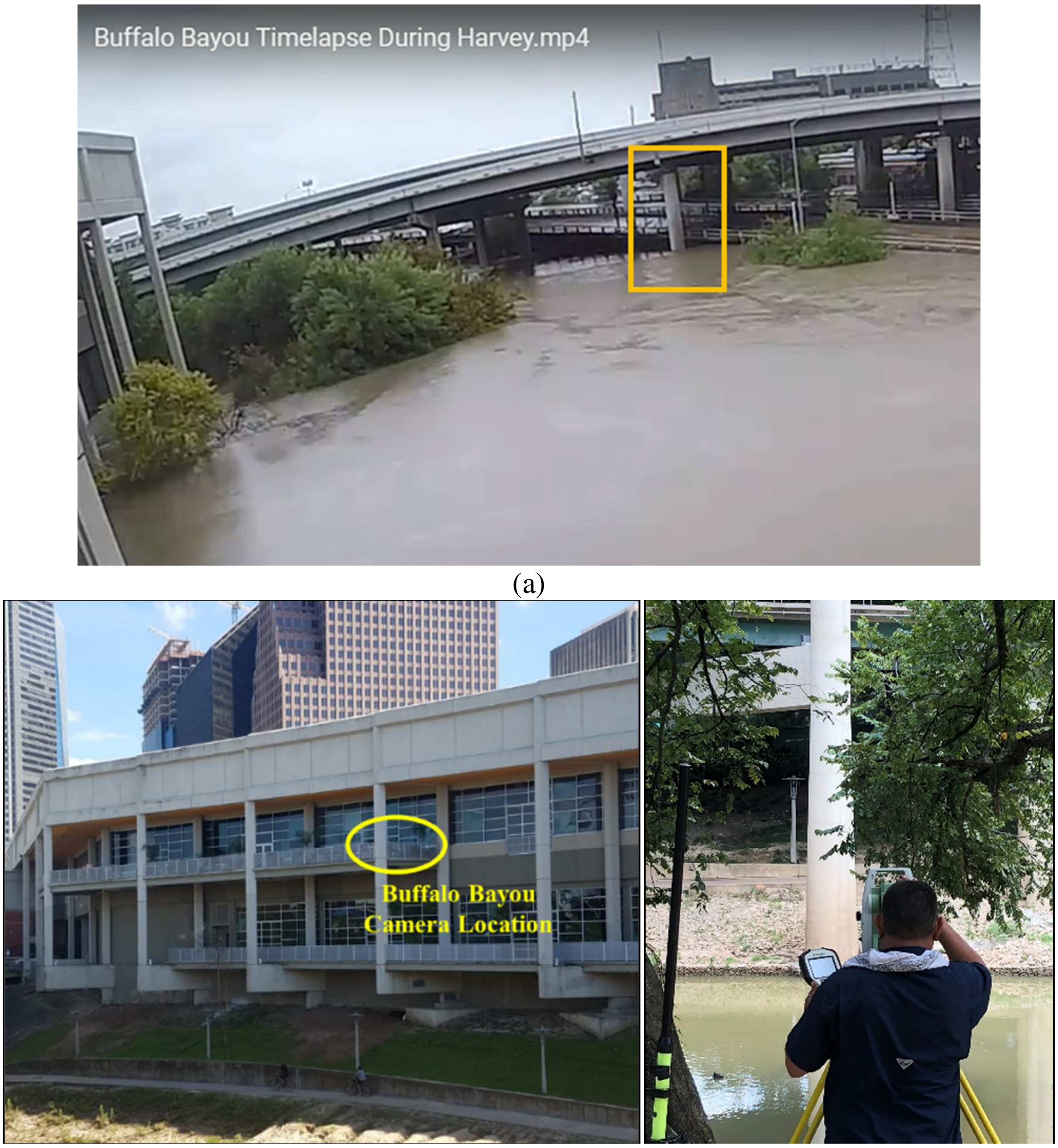
Buffalo Bayou Timelapse During Harvey.mp4
Buffalo Bayou Camera Location

(a)

(b) (c)

Figure 13. Hurricane Harvey Case Study in Buffalo Bayou, Houston: (a) Image of flooding Memorial Drive overpass from camera (image permission from Teddy Vandenberg), (b) Camera location on Bayou Place Offices building, and (c) Survey of bridge pier and Buffalo Bayou by T. Baker Smith, LLC.

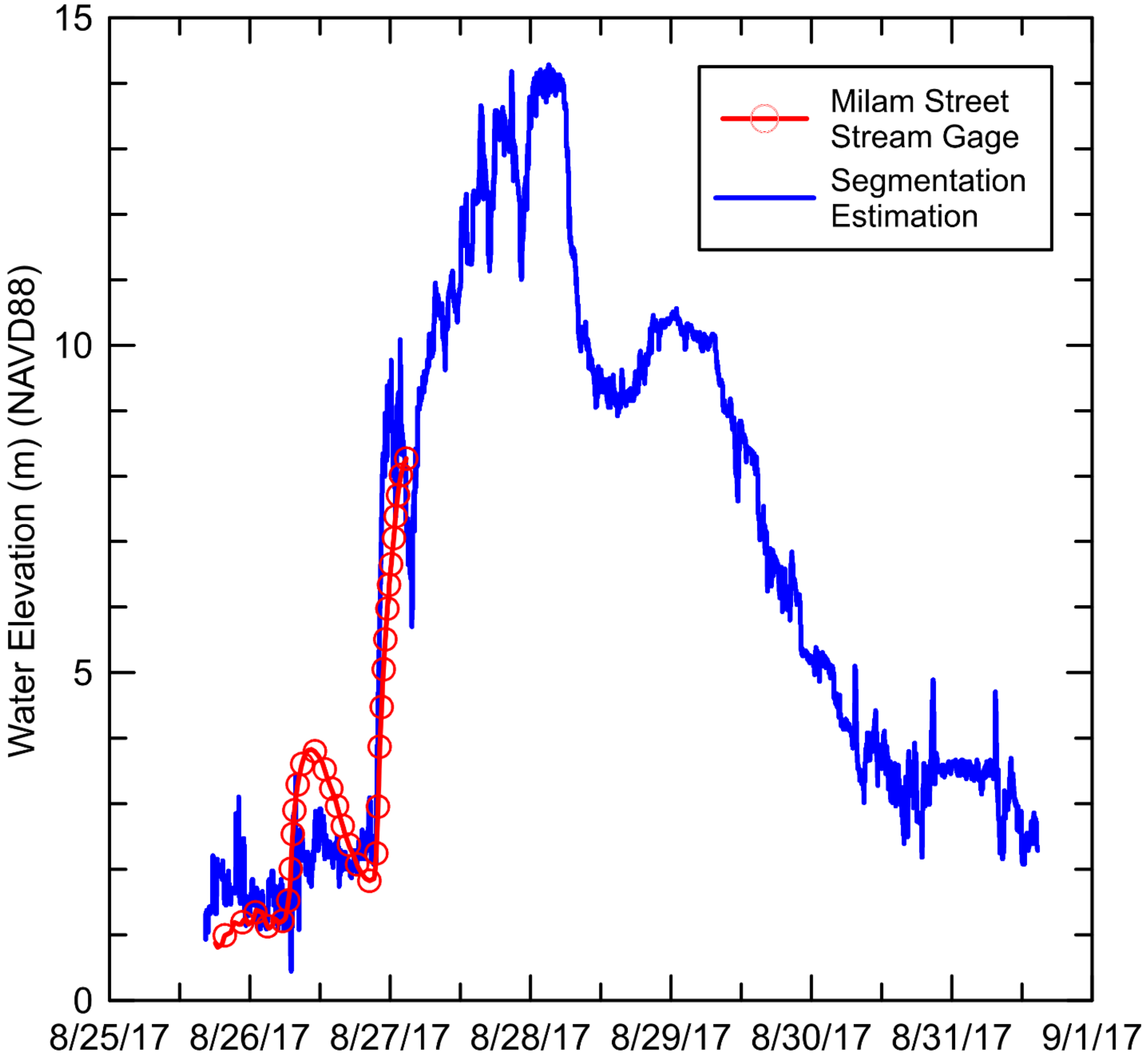

Figure 14. Comparison of reconstructed hydrograph and Milam Street Stream Gage.